JOURNAL OF COMPUTATIONAL PHYSICS 115, 27–42 (1994)

An Advection Algorithm and an Atmospheric Airflow Application

PÄR HOLMGREN

Department of Meteorology, Uppsala University, Box 516, S-751 20 Uppsala, Sweden

Received May 18, 1993; revised March 7, 1994

A new advection algorithm based on the scheme by MacCormack has been implemented in the atmospheric meso-γ-scale model developed at the Department of Meteorology, Uppsala University. Prior to the implementation of the scheme, it was first tested in a simple advection model and in a shock wave model. The meso-γ-scale model used to have a simple forward upstream scheme. The new scheme gives much less numerical dissipation compared to the upstream scheme, and this may cause reflection at the upper boundary. This is clearly seen in a simulation of airflow over bell-shaped terrain. This reflection was avoided when the model was provided with an upper boundary condition, proposed by Klemp and Durran, that permits radiation of internal gravity waves. In a simulation of a sea breeze circulation, the new scheme gives a sharper sea breeze front. It also gives a higher maximum wind speed and the maximum is reached earlier in the simulation. The grid in the meso-γ-scale model has also been staggered, the velocity components have all been moved a half grid interval from the location of the thermodynamic variables in the direction of the respective velocity component.

1. INTRODUCTION

Advection is one of the most important physical processes in the atmosphere. Hence there is a need to have as good advection scheme as possible in a numerical model of the atmosphere. This is even more important in a dispersion model with chemistry included. What is then meant by a *good* scheme? A "perfect" advection scheme should fulfill four important criteria. It should be conservative, i.e., the model must not change the total content of any conservative property, e.g., mass due to the advection scheme itself; the scheme should be positive-definite, a variable which is defined positive must remain positive; furthermore, the scheme must not introduce any new over- or undershoots; and, last but not least, amplitude as well as phase errors should be as small as possible. Together with these four criteria, computational efficiency must for many applications also be taken into consideration. In the literature a number of methods for the numerical solution of the advection can be found. Reviews and comparisons can be found in, e.g., [1 or 2].

The MIUU-model have used the *forward-upstream* scheme for the advection

$$\phi_j^{n+1} = \phi_j^n - \alpha(\phi_j^n - \phi_{j-1}^n), \quad \text{if} \quad U > 0 \tag{1a}$$

$$\phi_j^{n+1} = \phi_j^n - \alpha(\phi_{j+1}^n - \phi_j^n), \quad \text{if} \quad U < 0, \tag{1b}$$

where α is $U\,\Delta t/\Delta x$, U is the velocity, t is time, and x is length. This scheme is conservative, positive-definite, and monotone. However, the scheme is associated with large numerical dissipation so amplitude errors are often large and in some cases that is also true for the phase errors as well. Along with the forward-upstream scheme, the Lax–Wendroff scheme was one of the first used in atmospheric models using the finite difference method. One step forward in time is here determined by

$$\phi_j^{n+1} = \phi_j^n - \alpha(\phi_{j+1/2}^{n+1/2} - \phi_{j-1/2}^{n+1/2}), \tag{2a}$$

where the intermediate value is obtained from

$$\phi_{j+1/2}^{n+1/2} = \frac{1}{2}(\phi_{j+1}^n + \phi_j^n) - \frac{\alpha}{2}(\phi_{j+1}^n - \phi_j^n). \tag{2b}$$

For meteorological applications it is interesting to study how this scheme was further improved by Gadd [3, 4], who instead of (2a) used

$$\phi_j^{n+1} = \phi_j^n - \alpha\left\{(1+a)(\phi_{j+1/2}^{n+1/2} - \phi_{j-1/2}^{n+1/2}) - \frac{a}{3}(\phi_{j+3/2}^{n+1/2} - \phi_{j-3/2}^{n+1/2})\right\}, \tag{3}$$

where a is a weight for the finite difference approximations to the spatial derivative. The intermediate value was still obtained from (2b). It reduces to the Lax–Wendroff scheme if $a = 0$. Gadd's scheme was in its turn then slightly modified by [5–6]. The lax–Wendroff scheme is a so-called two-step method and a variation of this is the scheme proposed by

581/115/1-3

0021-9991/94 $6.00

MacCormack [7]. This method alternately uses forward and backward differences for the two steps. The algorithm is

$$\phi_j^{n+1} = \tfrac{1}{2}\{\phi_j^n + \phi_j^{\overline{n+1}} - \alpha(\phi_j^{\overline{n+1}} - \phi_{j-1}^{\overline{n+1}})\}, \tag{4a}$$

where the preliminary value is

$$\phi_j^{\overline{n+1}} = \phi_j^n - \alpha(\phi_{j+1}^n - \phi_j^n). \tag{4b}$$

In the linear case, that is if U and ϕ are independent of each other, MacCormack and Lax–Wendroff are identical:

$$\phi_j^{n+1} = \phi_j^n - \frac{\alpha}{2}(\phi_{j+1}^n - \phi_{j-1}^n) + \frac{\alpha^2}{2}(\phi_{j+1}^n - 2\phi_j^n + \phi_{j-1}^n). \tag{5}$$

This is a scheme of order 2.2; i.e., it is of second order in both space and time. Another way to improve a scheme to a higher order in time is to use data from more than one time level. An example is the frequently used *leapfrog* scheme, which is also of the order 2.2,

$$\phi_j^{n+1} = \phi_j^{n-1} - \alpha(\phi_{j+1}^n - \phi_{j-1}^n). \tag{6}$$

This scheme needs information from timestep $n-1$, as well as from timestep n. Hence, one must store all the data from $n-1$, and especially if the model includes chemistry this means quite large storage requirements. Furthermore, this scheme may give a nonphysical solution, the computational mode, or decoupling of time-levels, as the value of a certain variable does not depend on the value of the same variable in the previous timestep. The solution may "jump" between two different developments. In order to suppress this separation of the solutions between odd and even timesteps either an occasional forward timestep or some kind of time filter has to be used. An occasional forward timestep means that the scheme no longer is of the second order in time. If a time filter is used on the other hand timestep $n-2$ must also be taken into consideration,

$$\bar{\phi}_j^{n-1} = \phi_j^{n-1} + \mu(\bar{\phi}_j^{n-2} - 2\phi_j^{n-1} + \phi_j^n), \tag{7}$$

where μ is the filtering weight. If we are using this filter, this will demand even more computer storage as well as computer time.

The leapfrog scheme can be modified to a higher order in space, leapfrog4,

$$\phi_j^{n+1} = \phi_j^{n-1} - \alpha\{\tfrac{4}{3}(\phi_{j+1}^n - \phi_{j-1}^n) - \tfrac{1}{6}(\phi_{j+2}^n - \phi_{j-2}^n)\}, \tag{8}$$

where five gridpoints are used instead of three when computing the next timestep.

The next section presents a new advection scheme, its accuracy, and its numerical stability. The third section gives some results from two quite simple models, whereas the behaviour of the scheme in a more complex atmospheric model is described in the fourth section. Conclusions and discussion are found in the closing section.

2. THE NEW ADVECTION SCHEME

2.1. *The Improved MacCormack Advection Scheme*

An improvement of the MacCormack scheme (4) involves a change both to the first and the second step. This can be done in a number of ways; the three most obvious are the following:

In the first one, MC2a, gridpoints *further outward* are taken into consideration:

$$\phi_j^{n+1} = \frac{1}{2}\left\{\phi_j^n + \phi_j^{\overline{n+1}} - \alpha[1+a](\phi_j^{\overline{n+1}} - \phi_{j-1}^{\overline{n+1}}) + \frac{\alpha a}{2}(\phi_j^{\overline{n+1}} - \phi_{j-2}^{\overline{n+1}})\right\} \tag{9a}$$

$$\phi_j^{\overline{n+1}} = \phi_j^n - \alpha[1+a](\phi_{j+1}^n - \phi_j^n) + \frac{\alpha a}{2}(\phi_{j+2}^n - \phi_j^n). \tag{9b}$$

Another way is to instead use gridpoints on *both sides* of the original ones, MC2b,

$$\phi_j^{n+1} = \frac{1}{2}\left\{\phi_j^n + \phi_j^{\overline{n+1}} - \alpha[1+a](\phi_j^{\overline{n+1}} - \phi_{j-1}^{\overline{n+1}}) + \frac{\alpha a}{3}(\phi_{j+1}^{\overline{n+1}} - \phi_{j-2}^{\overline{n+1}})\right\} \tag{10a}$$

$$\phi_j^{\overline{n+1}} = \phi_j^n - \alpha[1+a](\phi_{j+1}^n - \phi_j^n) + \frac{\alpha a}{3}(\phi_{j+2}^n - \phi_j^n). \tag{10b}$$

And a third way is to take gridpoints *towards the center* into consideration, MC2c.

$$\phi_j^{n+1} = \frac{1}{2}\left\{\phi_j^n + \phi_j^{\overline{n+1}} - \alpha[1+a](\phi_j^{\overline{n+1}} - \phi_{j-1}^{\overline{n+1}}) + \frac{\alpha a}{2}(\phi_{j+1}^{\overline{n+1}} - \phi_{j-1}^{\overline{n+1}})\right\} \tag{11a}$$

$$\phi_j^{\overline{n+1}} = \phi_j^n - \alpha[1+a](\phi_{j+1}^n - \phi_j^n) + \frac{\alpha a}{2}(\phi_{j+1}^n - \phi_{j-1}^n). \tag{11b}$$

If $a = \frac{1}{3}$ in the first scheme, it becomes a scheme of fourth order in space, as shown in the next subsection. For MC2b the value of a should be $\frac{1}{2}$, then this also becomes a scheme

of fourth order. For the third scheme, however, only third order can be obtained and that is independent of a. As will be seen the results from the first two schemes are very similar, but as more gridpoints are involved in MC2b, seven instead of five in MC2a, the boundary conditions will be simpler with the first scheme. When one of these schemes, or the original MacCormack scheme, is used the direction of the numerical stencil should be alternated; i.e., in the case of MC2a (9) the grid points j, $j+1$, and $j+2$ should be used in the preliminary time step and j, $j-1$, and $j-2$ in the second step and vice versa every other time step. In two or three dimensions the advection in the different directions should also be alternated. These things are done to avoid systematical errors.

The MacCormack scheme, and its cousin Lax–Wendroff, have not been used so often in meteorological models but some recent applications of the MacCormack scheme can be found in [8, 9]. Reference [10] presented results suggesting that the Lax–Wendroff scheme has damping and phase properties which are unacceptably inferior to those of the leapfrog and other schemes. This implication is, however, false, as [3] pointed out. The scheme studied by [10] was not the true Lax–Wendroff scheme, since there was no spatial staggering at the intermediate time levels, $n+\frac{1}{2}$. Unfortunately this erroneous assessment has had a lasting influence within parts of the meteorological science community.

2.2. *The Accuracy of the New Scheme*

If we apply MC2a to the simple linear advection equation

$$\frac{\partial \phi}{\partial t} = -U\frac{\partial \phi}{\partial x}, \tag{12}$$

we obtain the expression

$$\begin{aligned}
2(\phi_j^{n+1}-\phi_j^n) = &-\alpha[1+a](\phi_{j+1}-\phi_j)+\alpha a(\phi_{j+2}-\phi_j)/2\\
&-\alpha[1+a]\{\phi_j-\alpha[1+a](\phi_{j+1}-\phi_j)\\
&+\alpha a(\phi_{j+2}-\phi_j)/2\}\\
&+\alpha[1+a]\{\phi_{j-1}-\alpha[1+a](\phi_j-\phi_{j-1})\\
&+\alpha a(\phi_{j+1}-\phi_{j-1})/2\}\\
&+\frac{\alpha a}{2}\{\phi_j-\alpha[1+a](\phi_{j+1}-\phi_j)\\
&+\alpha a(\phi_{j+2}-\phi_j)/2\}\\
&-\frac{\alpha a}{2}\{\phi_{j-2}-\alpha[1+a](\phi_{j-1}-\phi_{j-2})\\
&+\alpha a(\phi_j-\phi_{j-2})/2\},
\end{aligned} \tag{13}$$

where all the terms on the right-hand side are at timestep n.

The coefficients for the α-terms are at the respective gridpoints:

$$\begin{aligned}
&a/2 \text{ in } \phi_{j+2}, \qquad -(1+a) \text{ in } \phi_{j+1},\\
&1+a \text{ in } \phi_{j-1}, \qquad -a/2 \text{ in } \phi_{j-2}.
\end{aligned}$$

The right-hand side in Eq. (13) should equal $-2\alpha\,\Delta x\,\phi'$. If we now use common Taylor expansion around ϕ_j, neglecting terms of order Δx^5 or higher, we obtain

$$\begin{aligned}
&2a\,\Delta x\,\phi' + \frac{4a}{3}\Delta x^3\,\phi''' - 2(1+a)\,\Delta x\,\phi' - \frac{1+a}{3}\Delta x^3\,\phi'''\\
&\quad = -2\Delta x\,\phi' + \frac{3a-1}{3}\Delta x^3\,\phi'''
\end{aligned}$$

and from this we see that the choice of a should be $\frac{1}{3}$. The new scheme is thus of fourth-order accuracy in space, but it is still of second order in time.

2.3. *The Numerical Stability of the New Scheme*

If we use the difference operators

$$\begin{aligned}
D_+\phi_j^n &= (\phi_{j+1}^n-\phi_j^n)/\Delta x\\
D_-\phi_j^n &= (\phi_j^n-\phi_{j-1}^n)/\Delta x\\
D_0\phi_j^n &= (\phi_{j+1}^n-\phi_{j-1}^n)/2\Delta x\\
D_{00}\phi_j^n &= (\phi_{j+2}^n-\phi_{j-2}^n)/4\Delta x
\end{aligned} \tag{14}$$

for the horizontal derivative $\partial/\partial x$ and

$$\begin{aligned}
D_+D_-\phi_j^n &= (\phi_{j+1}^n-2\phi_j^n+\phi_{j-1}^n)/\Delta x^2\\
D_-D_0\phi_j^n &= (\phi_{j+1}^n-\phi_j^n-\phi_{j-1}^n+\phi_{j-2}^n)/2\Delta x^2\\
D_+D_0\phi_j^n &= (\phi_{j+2}^n-\phi_{j+1}^n-\phi_j^n+\phi_{j-1}^n)/2\Delta x^2\\
D_0D_0\phi_j^n &= (\phi_{j+2}^n-2\phi_j^n+\phi_{j-2}^n)/4\Delta x^2
\end{aligned} \tag{15}$$

for $\partial^2/\partial x^2$, it is possible to write

$$\begin{aligned}
2(\phi_j^{n+1}-\phi_j^n) = &-U\,\Delta t\,(\tfrac{4}{3}D_+\phi_j^n-\tfrac{1}{3}D_0\phi_{j+1}^n\\
&+\tfrac{4}{3}D_-\phi_j^n-\tfrac{1}{3}D_0\phi_{j-1}^n)\\
&+U^2\,\Delta t^2(\tfrac{16}{9}D_+D_-\phi_j^n-\tfrac{4}{9}D_-D_0\phi_{j+1}^n\\
&-\tfrac{4}{9}D_+D_0\phi_{j-1}^n+\tfrac{1}{9}D_0D_0\phi_j)
\end{aligned} \tag{16}$$

for the linear advection equation (12). Here we have used $a=\frac{1}{3}$ in MC2a (9). If we then use

$$\begin{aligned}
D_+\phi_j^n + D_-\phi_j^n &= 2D_0\phi_j^n\\
D_0\phi_{j+1}^n + D_0\phi_{j-1}^n &= 2D_{00}\phi_j^n\\
D_-D_0\phi_{j+1} + D_+D_0\phi_{j-1} &= 2D_0D_0\phi_j
\end{aligned} \tag{17}$$

TABLE I

The Stability of the New Advection Scheme MC2a Depending on Different Wave Lengths and Courant Numbers

	0.0	0.1	0.2	0.3	0.4	0.5	0.6	0.7	0.8	0.9	1.0
$2\Delta x$	1.0000	0.9644	0.8578	0.6800	0.4311	0.1111	0.2800	0.7422	1.2756	1.8800	2.5556
$3\Delta x$	1.0000	0.9849	0.9416	0.8775	0.8089	0.7661	0.7928	0.9240	1.1621	1.4900	1.8916
$4\Delta x$	1.0000	0.9951	0.9814	0.9621	0.9431	0.9330	0.9434	0.9865	1.0724	1.2065	1.3889
$5\Delta x$	1.0000	0.9981	0.9929	0.9858	0.9790	0.9758	0.9805	0.9982	1.0338	1.0920	1.1761
$6\Delta x$	1.0000	0.9991	0.9968	0.9936	0.9906	0.9894	0.9918	1.0003	1.0173	1.0457	1.0877
$7\Delta x$	1.0000	0.9996	0.9983	0.9967	0.9952	0.9946	0.9960	1.0006	1.0098	1.0253	1.0485
$8\Delta x$	1.0000	0.9998	0.9991	0.9982	0.9974	0.9971	0.9979	1.0005	1.0056	1.0142	1.0272
$9\Delta x$	1.0000	0.9999	0.9995	0.9989	0.9985	0.9983	0.9988	1.0004	1.0035	1.0087	1.0166
$10\Delta x$	1.0000	0.9999	0.9996	0.9993	0.9990	0.9989	0.9992	1.0003	1.0024	1.0058	1.0111
$11\Delta x$	1.0000	0.9999	0.9998	0.9995	0.9993	0.9992	0.9995	1.0002	1.0017	1.0041	1.0078
$12\Delta x$	1.0000	1.0000	0.9998	0.9997	0.9996	0.9995	0.9997	1.0002	1.0011	1.0027	1.0051
$13\Delta x$	1.0000	1.0000	0.9999	0.9998	0.9997	0.9995	0.9998	1.0001	1.0008	1.0019	1.0036
$14\Delta x$	1.0000	1.0000	0.9999	0.9998	0.9997	0.9997	0.9998	1.0001	1.0006	1.0016	1.0029
$15\Delta x$	1.0000	1.0000	0.9999	0.9999	0.9998	0.9998	0.9999	1.0001	1.0005	1.0013	1.0024
$16\Delta x$	1.0000	1.0000	0.9999	0.9999	0.9998	0.9998	0.9999	1.0001	1.0004	1.0010	1.0019

we will obtain

$$\phi_j^{n+1} - \phi_j^n = -U\,\Delta t\,(\tfrac{4}{3}D_0\phi_j^n - \tfrac{1}{3}D_{00}\phi_j^n) + U^2\,\Delta t^2\,(\tfrac{8}{9}D_+D_-\phi_j^n - \tfrac{7}{18}D_0D_0\phi_j^n). \quad (18)$$

The Fourier transforms of these difference operators are

$$\begin{aligned} D_0 &\to i\sin(\omega\,\Delta x)/\Delta x \\ D_{00} &\to i\sin(2\omega\,\Delta x)/2\Delta x \\ D_+D_- &\to -4\sin^2(\omega\,\Delta x/2)/\Delta x^2 \\ D_0D_0 &\to -\sin^2(\omega\,\Delta x)/\Delta x^2. \end{aligned} \quad (19)$$

With these it is possible to transform (18) and we obtain

$$z = 1 - \frac{4}{3}\frac{U\,\Delta t}{\Delta x} i\sin\omega\,\Delta x + \frac{1}{6}\frac{U\,\Delta t}{\Delta x} i\sin 2\omega\,\Delta x - \frac{32}{9}\left(\frac{U\,\Delta t}{\Delta x}\right)^2 \sin^2\frac{\omega\,\Delta x}{2} + \frac{7}{18}\left(\frac{U\,\Delta t}{\Delta x}\right)^2 \sin^2\omega\,\Delta x, \quad (20)$$

where z is the amplification in each time step. If the scheme is stable then $|z| \leqslant 1$ for any $\omega\,\Delta x$.

By introducing $\lambda = U\,\Delta t/\Delta x$, $\gamma = \omega\,\Delta x$, using tri-

TABLE II

The Phase Velocity for the New Advection Scheme MC2a Depending on Different Wave Lengths and Courant Numbers

	0.0	0.1	0.2	0.3	0.4	0.5	0.6	0.7	0.8	0.9	1.0
$2\Delta x$	0.0000	0.0000	0.0000	0.0000	0.0000	0.0000	0.0000	0.0000	0.0000	0.0000	0.0000
$3\Delta x$	1.0000	0.6316	0.6674	0.7324	0.8326	0.9662	1.1036	1.1930	1.2144	1.1881	1.1386
$4\Delta x$	1.0000	0.8556	0.8760	0.9099	0.9566	1.0134	1.0740	1.1287	1.1674	1.1845	1.1807
$5\Delta x$	1.0000	0.9351	0.9467	0.9658	0.9918	1.0234	1.0586	1.0942	1.1264	1.1514	1.1664
$6\Delta x$	1.0000	0.9673	0.9747	0.9868	1.0032	1.0234	1.0466	1.0713	1.0960	1.1188	1.1378
$7\Delta x$	1.0000	0.9820	0.9871	0.9954	1.0068	1.0209	1.0374	1.0555	1.0745	1.0933	1.1111
$8\Delta x$	1.0000	0.9895	0.9931	0.9992	1.0076	1.0180	1.0303	1.0441	1.0590	1.0744	1.0898
$9\Delta x$	1.0000	0.9935	0.9963	1.0009	1.0073	1.0154	1.0250	1.0358	1.0477	1.0604	1.0734
$10\Delta x$	1.0000	0.9958	0.9980	1.0017	1.0068	1.0132	1.0208	1.0296	1.0393	1.0498	1.0608
$11\Delta x$	1.0000	0.9972	0.9990	1.0020	1.0061	1.0113	1.0176	1.0248	1.0329	1.0417	1.0510
$12\Delta x$	1.0000	0.9981	0.9996	1.0020	1.0055	1.0098	1.0150	1.0211	1.0279	1.0353	1.0434
$13\Delta x$	1.0000	0.9987	0.9999	1.0020	1.0049	1.0086	1.0130	1.0181	1.0239	1.0303	1.0373
$14\Delta x$	1.0000	0.9990	1.0000	1.0019	1.0044	1.0075	1.0113	1.0157	1.0207	1.0263	1.0323
$15\Delta x$	1.0000	0.9993	1.0000	1.0018	1.0039	1.0066	1.0099	1.0138	1.0182	1.0230	1.0283
$16\Delta x$	1.0000	0.9995	1.0000	1.0016	1.0035	1.0059	1.0088	1.0122	1.0160	1.0203	1.0250

gonometric identities and square the real part and the imaginary part separately we obtain

$$|z|^2 = \left(1 - \frac{16\lambda^2}{9}\right)^2 + \frac{32\lambda^2}{9}\cos\gamma - \frac{512\lambda^4}{81}\cos\gamma + \frac{256\lambda^4}{81}\cos^2\gamma + \frac{23\lambda^2}{9}\sin^2\gamma - \frac{112}{81}\lambda^4\sin^2\gamma - \frac{8}{9}\lambda^2\sin^2\gamma\cos\gamma + \frac{112\lambda^4}{81}\sin^2\gamma\cos\gamma + \frac{\lambda^2}{9}\sin^2\gamma\cos^2\gamma + \frac{49}{324}\lambda^4\sin^4\gamma. \tag{21}$$

Since all the sine terms are either raised to 2 or 4, they are easy to convert to cosine terms, while at the same time putting $\cos\gamma = \psi$, where $|\psi| \leqslant 1$, the final expression becomes

$$|z|^2 = 1 - \lambda^2 + \tfrac{625}{324}\lambda^4 + \tfrac{24}{9}\lambda^2\psi - \tfrac{400}{81}\lambda^4\psi - \tfrac{22}{9}\lambda^2\psi^2 + \tfrac{229}{54}\lambda^4\psi^2 + \tfrac{8}{9}\lambda^2\psi^3 - \tfrac{112}{81}\lambda^4\psi^3 - \tfrac{1}{9}\lambda^2\psi^4 + \tfrac{49}{324}\lambda^4\psi^4. \tag{22}$$

This somewhat cumbersome expression can be compared to the corresponding expression for the original MacCormack scheme, which is just $|z|^2 = 1$.

Table I shows how the amplification of the new scheme depends on the wave length $\gamma = \omega\,\Delta x$ and the Courant number $\lambda = U\,\Delta t/\Delta x$. As can be seen in this table the scheme is stable if λ is kept less than about 0.7. This agrees with experiences for both linear and non linear cases.

Table II shows that the phase velocity, which we can obtain from (20), is also reasonably close to unity if λ is kept less than about 0.7 and if we are dealing with wavelengths that are $6\Delta x$ or longer.

3. NUMERICAL TESTS

3.1. *Description of the Tests*

To see how these variations of the MacCormack scheme and other advection schemes behave, they have been tested in two different ways. The first is a simple *linear* advection in one dimension with 360 gridpoints and with periodic boundary conditions. The advected shapes have been either a half sine curve, a triangle, or a rectangle. As they move along a circle we will not have any boundary problems.

The second test, described by [11], is a quite common way to see how different numerical schemes act in a *nonlinear* case. Here we use the equations of *Euler*, which describe the dynamics for an inviscid flow (hence neglecting the viscosity of air). The equations in one space dimension are

$$\frac{\partial \Gamma}{\partial t} + \frac{\partial F(\Gamma)}{\partial x} = 0, \tag{23}$$

where

$$\Gamma = (\rho, \rho u, \rho E)^{\mathrm{T}}$$

$$F(\Gamma) = (\rho u, \rho u^2 + p, (\rho E + p)u)^{\mathrm{T}},$$

where ρ is the density, u is the velocity, p is the pressure, and E is the total energy per unit mass. The variables relate to each other by

$$E = \tfrac{1}{2}u^2 + e, \qquad p = (\gamma - 1)\,\rho e,$$

where e is the internal energy per unit mass and γ is a constant, 1.4 for air.

Consider an infinitely thin and long pipe filled with air and a tightfitting plate in the middle of the pipe. If the pressure of the air is higher on one side of the plate a shock wave will go through the pipe if the plate is removed. This shock wave is nonlinear and can be used to see how the different numerical schemes behave in a nonlinear case. To the right of the plate the initial density is set to 0.125 and the pressure is 0.1. To the left the density 1.0 and the pressure 1.0 are used instead. The velocity is zero initially on both sides of the plate. Note that all variables are nondimensional and not expressed in SI-units. As the pipe not only is infinitely thin but also infinitely long, boundary conditions will not need to be considered in the numerical model, the pipe just need to be long enough for the shock wave not to reach the boundaries during the simulation. The values at the boundaries will remain the same during the whole integration.

The new advection schemes (9)–(11) were compared with the advection schemes mentioned earlier: forward-upstream (1), Lax–Wendroff (2), Gadd (3), MacCormack (4), leapfrog (6), and leapfrog (8). These schemes were applied to the conservative variables ρ, ρu, and ρE.

A numerical advection scheme of a higher order, without numerical dissipation, will produce oscillations, Gibb's phenomena, at discontinuities in the solution. This also occurs when the discontinuities are in the derivatives of the solution, e.g., advection of the half sine curve. In the latter case the discontinuities are in the first derivative in the corner points.

By applying some kind of filter these phenomena can be avoided. The simplest filters are either a spatial smoothing filter or a cutoff filter. In these simulations a filter suggested by [12] has been used; it is the same filter that is used in the MIUU meso-γ-model, which is described in the next section. If the peak region is sufficiently smooth this nonlinear filter smoothens out $2m\,\Delta x$ ripples by applying a local smoothing operator, without suppressing a possible peak value significantly. The filter is defined as

$$c_i^{n+1,k+1} = c_i^{n+1,k} + \frac{\kappa}{2}\{\Delta c_{i+1/2}^{n+1,k}(\mu_i^k + \mu_{i+1}^k) - \Delta c_{i-1/2}^{n+1,k}(\mu_i^k + \mu_{i-1}^k)\}$$
$$k = 0, 1, 2, \ldots, K_{\max}, \tag{24}$$

where the index k is an iteration index, $\kappa < \frac{1}{2}$ is a diffusion coefficient and μ_i is a mesh parameter which is set to 0 for all values of i before each iteration. Further variables in this filter are

$$\Delta c_{i+1/2} = c_{i+1} - c_i, \qquad S_{i+1} = \text{sign}(\Delta c_{i+1/2}).$$

By means of the sign function it is possible to detect $2m\,\Delta x$ ripples. If $S_j \neq S_{j+1}$ for a particular j, a local extremum is present. To see whether it is a true extremum, $S_{j-m}, \ldots, S_j$ must have the same sign, whereas $S_{j+1}, \ldots, S_{j+m}$ are all required to have the opposite sign. If this condition is not fulfilled, then all μ_i are reset to 1 in the interval with the nodes $j-m$ to $j+m$. If the sign condition holds, there is a true local extremum and the filtering process can be continued at x_{j+m}. The selective smoothing can be repeated several times. Here the values are set as $\kappa = 0.25$, $k = 2$, and $m = 1$ for filtering $2\Delta x$ waves and in some applications $\kappa = 0.25$, $k = 2$, and $m = 2$ for filtering $4\Delta x$ waves. The $4\Delta x$-filter produces $2\Delta x$-waves, so if this filter is used, the $2\Delta x$-filter must be used afterwards.

A different approach is to use a filter which takes away all values that are below or above a certain level. This is especially useful when it comes to avoiding negative values for, e.g., relative humidity or concentration. When using filters one must be careful to assure that the filter does not change the total content of the filtered variable, the filter must be *conservative*. This is especially crucial at the boundaries. It is important that the filter does not prevent a concentration from vanishing out through an outflow boundary. Conservation is assured by simply addings as much to the other gridpoints as is filtered away at the filtered gridpoint. Gridpoints at inflow boundaries are never filtered though.

3.2. *Results of the Linear Advection*

To integrate a meso-γ-scale model 24 h takes about 5000 iterations with a typical timestep of about 15 s. In these tests with simple linear advection the total number of iterations are about 10,000. The advecting velocity varied between 1 and 7 m/s giving a Courant number of 0.1 to 0.7. Both the $2\Delta x$-filter and the $4\Delta x$-filter were used in all integrations. In Fig. 1 the results with a velocity of 5 m/s, corresponding to a Courant number of 0.5, are shown for the forward-upstream scheme (1), Lax–Wendroff (2), Gadd (3), leapfrog4 (8), the original MacCormack scheme (4), and the three new versions of that scheme (9), (10), and (11).

Between each graph there are 3600 iterations, corresponding to five rotations around the circle with an advection of 5 m/s. Thus if the advection scheme is perfect all graphs should be exactly the same. This is obviously not the case when we use the upstream scheme. Already after five rotations the wave is very damped and after 15 rotations the wave is almost impossible to see. It appears as a straight line with a value slightly less than 0.1. There is also a phase error, as the maximum value for each wave is somewhat further to the left. The Lax–Wendroff scheme also loses some of the initial amplitude, and there are also disturbances to the left of the wave. These disturbances are not filtered as they are longer than $4\Delta x$; the whole circle is divided into 360 gridpoints. The figure only shows the result after five and 10 rotations. After another five rotations the errors were even larger, in fact too large for the curve to include in the plotted graph; some values were below -0.3. The Gadd scheme provides, as expected, a somewhat better result. Here we can see the wave after five, 10, and 15 rotations. The amplitude is closer to unity and the small disturbances are slightly smaller. The result for the leapfrog method is about the same as for the upstream method. The damping is slightly smaller, but the phase error is almost more evident, although here the maximum is pushed a little to the right for each rotation. The original MacCormack scheme gives exactly the same result as the Lax–Wendroff, which is what should be expected as they are identical in the linear case, just as Eq. (5) showed. The first two of the new schemes give results that are very similar. The amplitude of the wave is best conserved of all the schemes, and the small scale disturbances are slightly smaller than for both the original scheme and the scheme provided by Gadd. The disturbances are smallest when using MC2b, and in this case, advecting something around a circle, boundary problems do not appear. However, using these schemes in a limited area model, MC2a is easier to apply, as discussed earlier. The third of the new schemes, MC2c, was not of fourth order in space as the other two. This scheme gives a result which is quite similar to the one provided by Lax–Wendroff or the original MacCormack scheme.

3.3. *Results of the Shock Wave Test*

In the atmosphere we are usually dealing with nonlinear events. To test the advection schemes in the nonlinear case, they were applied to the shock wave simulation described earlier. The forward-upstream scheme was not applied to the shock wave test; instead another scheme with much numerical viscosity was used, the Lax–Friedrich scheme:

$$\phi_j^{n+1} = \frac{1}{2}(\phi_{j+1}^n + \phi_{j-1}^n) - \frac{\alpha}{2}(\phi_{j+1}^n - \phi_{j-1}^n). \qquad (25)$$

As we can see in Fig. 2 the result of this scheme does not look like a real shock wave, the pressure curve reminds us more of a downhill slope. In all the other cases a more accurate picture of the physics is obtained. Most cases expose small scale disturbances at the discontinuities. This is maybe most distinct for the Lax–Wendroff scheme, where a relatively large peak appears upstream of the shock wave front. This peak is also present in the Gadd simulation, although smaller, but here there is also a disturbance

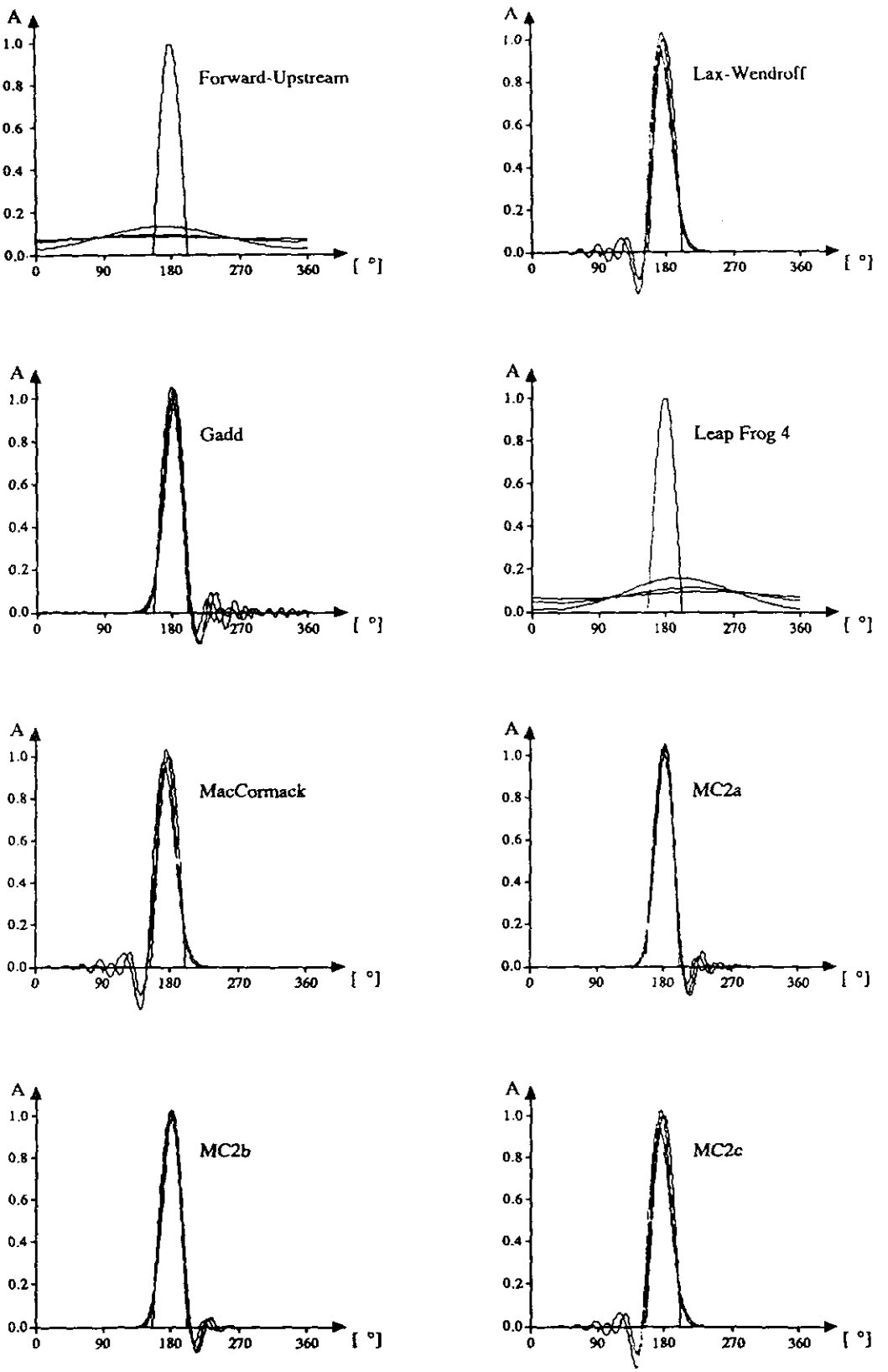

FIG. 1. Advection of a half sine curve along a circle according to the different schemes. The advecting velocity is 5 m/s. The curve has rotated five revolutions between each graph.

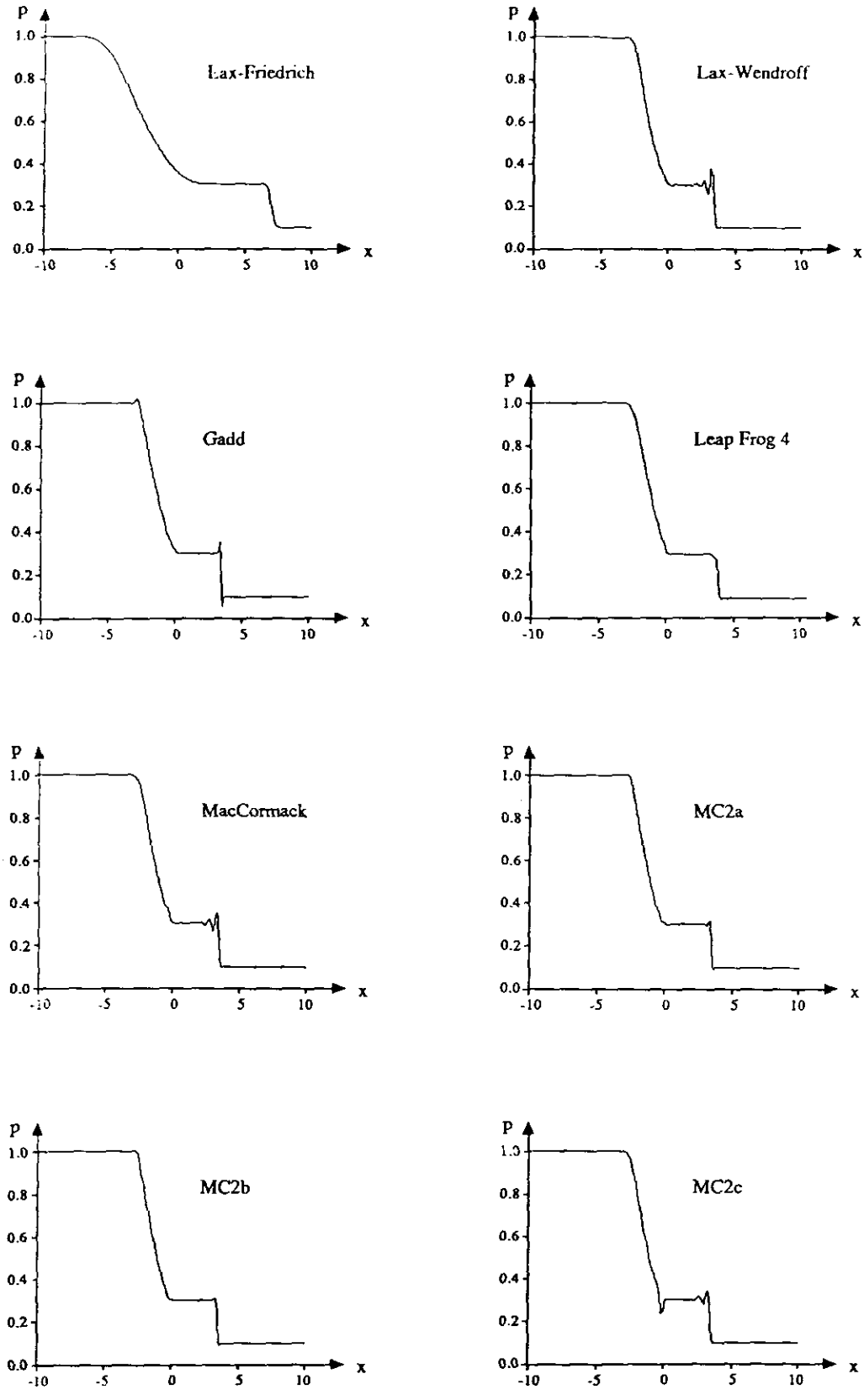

FIG. 2. The nondimensional pressure in the pipe after two time units as described by the various schemes.

downstream of the front. The leap frog scheme gives a very realistic result with just a trace of smoothing at the sharp corners. The MacCormack scheme gives a result that is quite similar to the Lax–Wendroff scheme, but they are *not* identical as we are now dealing with a nonlinear phenomenon. The disturbances provided by this scheme is somewhat smaller than the disturbances from the Lax–Wendroff scheme. Just as in the previous subsection the results from the two first of the new schemes are almost the same. Compared to the result from the leapfrog scheme they give slightly sharper corners but there are also hints of Gibb's phenomena, so it is actually a matter of taste to choose between MC2a, MC2b, and the leapfrog scheme. As stated before the leapfrog scheme demands storage of the old time steps and this can be quite demanding in a large three-dimensional model for the atmosphere into account. The third of the new schemes actually gives a worse result than the original MacCormack scheme.

4. THE NEW ADVECTION SCHEME IN THE MIUU MESO-γ-MODEL

4.1. *The MIUU Meso-γ-Model*

So far only advection in physically simple models has been studied; the next step is to introduce the new advection scheme in a physically more sophisticated model for studies of the atmosphere. At the Department of Meteorology, Uppsala University (MIUU), a three-dimensional numerical model for studies of atmospheric flow on the meso-γ-scale has been developed during the last decade [13]. Atmospheric flow on the meso-γ-scale has typical horizontal scales on the order of a few kilometers and a time scale of some hours. The turbulence closure scheme in the model was developed by [14] and is of the second order, level 2.5. Recently situations where the hydrostatic balance between gravity and the vertical pressure gradient force cannot be applied, i.e., nonhydrostatic effects, have been investigated [15, 16]. A recent application of the model can be found in [17].

Topography is introduced by the application of a terrain-following coordinate system with the vertical coordinate η, defined as

$$\eta = s\frac{z - z_g}{s - z_g}, \tag{26}$$

where s is the top of the model, z_g is the terrain height, and z is the height above sea level. The vertical gridpoints are spaced according to a relation which varies approximately logarithmically in the surface layer and linearly in the higher levels, i.e., in the same general manner as many important variables do, temperature, wind, etc. This is done with the coordinate transformation

$$\sigma = A\eta + B\ln\left(\frac{\eta + 1}{C}\right); \qquad \Delta\sigma = \text{const}, \tag{27}$$

where A, B, and C are constants. The reason for this transformation is that the accuracy of a finite-difference approximation is improved if the grid is defined in such a way that variables vary linearly with coordinates. In most applications the horizontal grid is also transformed, to increase the resolution in the central area. This transformation is usually done with either a gaussian or with an arctan transformation. An exponential expansion of the grid can also be used; i.e., the distance between two gridpoints is multiplied with a constant factor to obtain the distance between the next two gridpoints. The original differential equations are transformed into the new horizontal coordinate system and the grid is then equally spaced in the new coordinate system. These telescopic grid transformations allow high resolution in the area of interest but at the same time keep the lateral boundaries as far away as possible, in order to reduce the influence of possible errors made in the boundary conditions. The new set of basic equations in this transformed coordinate system then becomes

$$\frac{dU}{dt} = \left(\frac{s}{s - z_g}\right)^2 \frac{\partial}{\partial\eta}\left(K_M \frac{\partial U}{\partial\eta}\right) - fV_g - \Theta\left(\frac{\partial\Pi}{\partial x}\right)_{\eta = c} + g\frac{\eta - s}{s}\frac{\partial z_g}{\partial x} + fV \tag{28}$$

$$\frac{dV}{dt} = \left(\frac{s}{s - z_g}\right)^2 \frac{\partial}{\partial\eta}\left(K_M \frac{\partial V}{\partial\eta}\right) + fU_g - \Theta\left(\frac{\partial\Pi}{\partial y}\right)_{\eta = c} + g\frac{\eta - s}{s}\frac{\partial z_g}{\partial y} - fU \tag{29}$$

$$\frac{d\Theta}{dt} = \left(\frac{s}{s - z_g}\right)^2 \frac{\partial}{\partial\eta}\left(K_H \frac{\partial\Theta}{\partial\eta}\right) + \sigma_R, \tag{30}$$

where

$$\frac{d}{dt} = \frac{\partial}{\partial t} + U\frac{\partial}{\partial x} + V\frac{\partial}{\partial y} + W^*\frac{\partial}{\partial\eta}, \tag{31}$$

U and V are the new quasi horizontal wind components, W^* is the vertical wind in the terrain following coordinate system, Θ is the potential temperature, f is the Coriolis parameter, U_g and V_g are the geostrophic wind components, g is the acceleration of gravity, K_M and K_H are the turbulent exchange coefficients for momentum and heat, σ_r

is the radiative heating or cooling, and Π is the scaled pressure (Exner function) defined as

$$\Pi = c_p \left(\frac{p}{p_{00}} \right)^{R_d/c_p}. \tag{32}$$

In this expression p is the pressure, p_{00} is a reference pressure, c_p is the specific heat at constant pressure, and R_d is the gas constant for dry air. The equation of continuity in the transformed coordinates is

$$\frac{\partial U}{\partial x} + \frac{\partial V}{\partial y} + \frac{\partial W^*}{\partial \eta} = \frac{1}{s - z_g} \left(U \frac{\partial z_g}{\partial x} + V \frac{\partial z_g}{\partial y} \right). \tag{33}$$

4.2. *Staggering the Grid*

The MIUU model has prior to this been staggered only in the vertical direction. Turbulence is calculated at vertical levels between those where the rest of the variables are determined.

The calculation of the vertical wind, which is obtained from the continuity equation, will be improved if all the velocity components are also staggered. If we move all three components half a gridstep along each respective direction, the horizontal divergence of the horizontal wind components, instead of the velocity itself can be estimated in the "old" gridpoints. The staggered velocity components are shown in Fig. 3. The vertical velocity, w, will be at the same levels as the turbulence. Another major advantage of this is that two gridpoints next to each other can be used when calculating horizontal derivatives of thermodynamic variables in the equations for the velocity components. This is also the case for the dependence of the slope of the terrain,

$$\frac{\partial \Pi}{\partial x}, \frac{\partial \Pi}{\partial y}, \frac{\partial z_g}{\partial x}, \frac{\partial z_g}{\partial y},$$

in the equations of motion (28) and (29). This way of staggering the velocity gridpoints is usually called the Arakawa C-grid, and it is the grid that [18] recommends. An unstaggered grid may also have noise generation in the pressure field as a velocity change in one gridpoint is related to the pressure at the adjacent points, but not at the central point. Thus the proper geostrophic adjustment cannot occur on the smallest scale with an unstaggered grid. This problem is handled by a staggered grid; the C-grid configuration deals with this process most efficiently.

There are some drawbacks, however. The calculation of advection of the variables needs the velocity at the gridpoint of the respective variable, and when calculating the Coriolis force the two horizontal wind components are needed at the same place. This has to be solved by averaging over two or four gridpoints.

Another problem is that the lower boundaries for the different velocity components appears at different locations. We use a no-slip boundary condition for u and v; that is, they are set to zero at the ground and want to have the possibility to give the temperature at the ground as input. This means that the lowest grid level for w will be situated below the ground. As we want the velocity to be zero at the ground, we will have to extrapolate a value for w_1 from w_2 and "$w_{1.5}$," which is a nonexisting value at the ground that we want to be identical to zero,

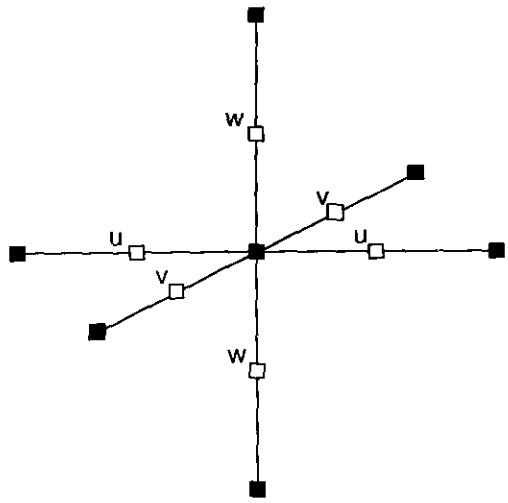

FIG. 3. The C-grid. The three velocity components are staggered half a grid step along each respective direction.

$$w_1 = -\Delta h_1 / \Delta h_2 \, w_2, \tag{34}$$

where Δh_1 is the height below the ground where the first grid level is situated and Δh_2 is the height above the ground for the second grid level.

In the horizontal directions the velocity components are at the outermost gridpoints in the respective direction; i.e., if the thermodynamic variables are located at i times j gridpoints, we have to have u in $i+1$ times j and v in i times $j+1$.

4.3. *The Upper Boundary Condition*

An upper boundary condition that permits internal gravity wave radiation in numerical mesoscale models, proposed by [19] has been incorporated in the model. In a hydrostatic model the gravity waves appear mainly in the vertical direction. There is a great difference between horizontal and vertical gravity waves. By using upstream differences at the lateral boundaries, outward propagating wave energy can be transmitted. This is not the case in the vertical direction.

Consider the simplest set of equations that support gravity wave propagation: the linear, two-dimensional,

hydrostatic, Boussinesq equations for a uniform mean state in the absence of Coriolis effects:

$$\frac{\partial u}{\partial t} + U\frac{\partial u}{\partial x} + \Theta\frac{\partial \pi}{\partial x} = 0 \tag{35}$$

$$\frac{\partial \theta}{\partial t} + U\frac{\partial \theta}{\partial x} + \frac{d\Theta}{dz}w = 0 \tag{36}$$

$$\Theta\frac{\partial \pi}{\partial z} - g\frac{\theta}{\Theta} = 0 \tag{37}$$

$$\frac{\partial u}{\partial x} + \frac{\partial w}{\partial z} = 0. \tag{38}$$

The basic wave propagation characteristics for this system of equations are best illustrated by considering the dispersion equation produced by disturbances, periodic in time and space,

$$\xi(x, z, t) = \tilde{\xi}(k_x, l, \omega)\exp[i(k_x x + lz - \omega t)], \tag{39}$$

where k_x and l are the horizontal and vertical wavenumbers, ω is the frequency. The existence of a nontrivial homogeneous solution requires that

$$\omega = k_x(U \pm C), \tag{40}$$

where $C = N/|l|$ and $N^2 = (g/\Theta)(d\Theta/dz)$, N is the Brunt–Väisälä frequency, and C is the intrinsic horizontal phase speed. Horizontal gravity wave propagation is characterized by the horizontal phase speed

$$C_{px} = \frac{\omega}{k_x} = U \pm C \tag{41}$$

and the horizontal group velocity

$$C_{gx} = \frac{\partial \omega}{\partial k_x} = U \pm C. \tag{42}$$

Thus these are the same for each pair of wavenumbers (k_x, l). This means that we can use the upstream scheme at the lateral boundaries to radiate the horizontal gravity waves. This is not the case at the top of the model. The vertical phase speed C_{pz} and group velocity C_{gz} are given by

$$C_{pz} = \frac{\omega}{l} = \frac{k_x}{l}(U \pm C) \tag{43}$$

$$C_{gz} = \frac{\partial \omega}{\partial l} = -\left(\pm\frac{k_x}{l}C\right). \tag{44}$$

These expressions are different from one another and, furthermore, if $C > U$ they have the opposite sign. This means that if wave energy is to be allowed to pass upward through the upper boundary, disturbances would have to be advected into the domain from above. Consequently, as [19] notes, the implementation of a vertical wave advection boundary condition at the upper boundary would require the use of numerically unstable downstream differences whenever gravity waves are present with phase speeds greater than the mean wind.

If we consider linear disturbances of the form

$$\xi(x, z, t) = \tilde{\xi}(k_x, z, \omega)\exp[i(k_x x - \omega t)] \tag{45}$$

and substitute these into (35)–(38), we obtain the wave equation for an atmosphere with constant wind speed and stability:

$$\frac{\partial^2 \hat{w}}{\partial z^2} + \frac{N^2}{(U - C_{px})^2}\hat{w} = 0. \tag{46}$$

The solutions to this wave equation describe the vertically propagating gravity wave modes and may be written

$$\hat{w} = A\exp\{i\,\mathrm{sign}(k_x)\,Nz/(U - C_{px})\} + B\exp\{-i\,\mathrm{sign}(k_x)\,Nz/(U - C_{px})\}. \tag{47}$$

As established by [20], the term with coefficient A corresponds to upward energy transport, while the term with coefficient B produces downward transport. Depending on the sign of $(U - C_{px})$, the corresponding vertical momentum flux may be either positive or negative.

Wave reflection at the top will be suppressed if $B = 0$ for all propagating modes. This is fulfilled if

$$\frac{\partial \hat{w}}{\partial z} = \frac{i\,\mathrm{sign}(k_x)N}{U - C_{px}}\hat{w}. \tag{48}$$

Another expression for this vertical gradient can be obtained by transforming the variables according to (45) and combining (35) and (38):

$$\frac{\partial \hat{w}}{\partial z} = -ik_x\hat{u} = \frac{ik_x}{U - C_{px}}\Theta\hat{\pi}. \tag{49}$$

If the right-hand side of these expressions are put equal the desired upper boundary condition for the pressure π, the perturbation Exner function, depending on the vertical velocity w will be

$$\hat{\pi} = \frac{N}{|k_x|\Theta}\hat{w}. \tag{50}$$

This expression differs from the expression derived by [19] by the constant factor c_p as they use

$$\Pi = \left(\frac{p}{p_{00}}\right)^{R_d/c_p} \tag{51}$$

as the definition for the Exner function instead of (32) which is used in the MIUU model.

In three dimensions with a mean wind component V in the y direction we will obtain

$$\hat{\pi} = \frac{N}{\Theta\sqrt{k_x^2 + k_y^2}}\hat{w}, \tag{52}$$

where k_y is the wave number in the y direction. This expression requires a two-dimensional Fourier transform along the upper surface of the model domain.

If we also take nonhydrostatic and Coriolis forces into consideration, the correct linear radiation condition becomes significantly more complicated:

$$\hat{\pi} = \frac{N}{\Theta\sqrt{k_x^2 + k_y^2}}\sqrt{1 - [k_x U + k_y V - \omega]^2/N^2}$$

$$\times\sqrt{1 - (f^2/[k_x U + k_y V - \omega]^2)}\,\hat{w}. \tag{53}$$

The influences of nonhydrostatic and rotational effects appear in the first and second square roots, respectively and permit the vertical radiation of wave energy only for

$$f^2 < (k_x U + k_y V - \omega)^2 < N^2. \tag{54}$$

For nearly stationary disturbances, such as in a mountain wave simulation, ω can be neglected. For propagating disturbances, however, this expression becomes ambiguous since we then need to have the frequencies associated with each pair of wavenumbers. The application would need the evaluation of Laplace transforms for which the past history of the flow at the boundary must be stored. Reference [19] concludes that if a boundary condition which radiates most of the transient and steady internal gravity wave energy and which is also easy to apply in a numerical model is required, the square roots in (53) can be ignored, which leads us back to (52).

4.4. *Results with Bell-Shaped Terrain*

As described by [16] the model was applied to simulate stably stratified airflow over mesoscale bell-shaped mountain ridges. In this study both the old forward-upstream scheme and the new version of the MacCormack scheme (9) were used and the simulations were done in two dimensions; i.e., the mountain ridge has an infinite length in the direction perpendicular to the airflow. The Forester filter described above for both $2\Delta x$ and $4\Delta x$ waves was applied in all simulations.

A situation with flow disturbances in a fluid with a uniform velocity $U = 10$ m/s and a buoyancy frequency N which is given by $N^2 = (g/\Theta)(d\Theta/dz)$ is studied. With a vertical temperature gradient of 3 K/km, N is thus about 0.01. The horizontal length scale or the ridge half width L is 10 km. This means that the ratio U/N is in the order of 1 km, i.e., about one-tenth of L. This corresponds to a typical case in the *hydrostatic nonrotating regime*, using the terminology of [21]. The wind field over the mountain ridge shows a clear vertical wave propagation with a wave length of about 2π km, which is just what we should expect.

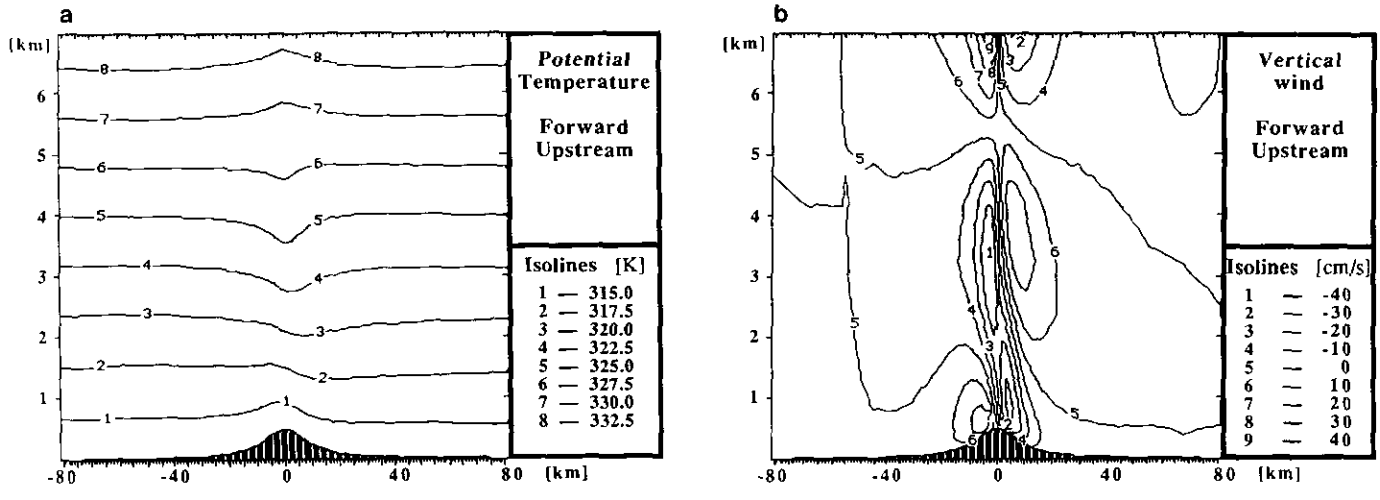

FIG. 4. (a) Cross section of the simulated potential temperature Θ for flow over a bell-shaped ridge by the upstream model. The shadowed section refers to surface terrain. The half width of the bell shaped ridge L is 10 km, the ridge crest height H is 1000 m, the geostrophic wind U_g is 10 m/s, and the lapse rate $d\Theta/dz$ is 1 K/km. (b) Same as in Fig. 4a but for the vertical wind speed w.

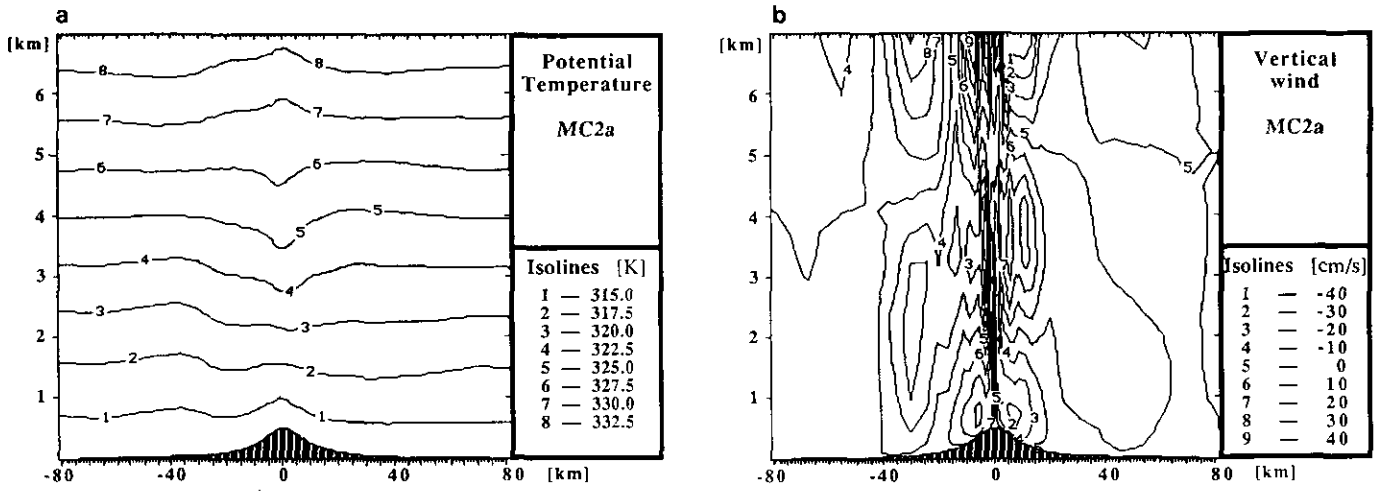

FIG. 5. (a) Same as Fig. 4a but with the new advection scheme MC2a. (b) Same as Fig. 4b but with the new advection scheme MC2a.

The potential temperature and vertical wind fields for the upstream model are shown in Figs. 4a and b. If the new scheme is used instead problems appear. Figure 5a shows a wave in the temperature field upstream of the mountain ridge and the vertical wind field in Fig. 5b looks very sprawling. Furthermore the values range from about -0.7–0.6 m/s when the new scheme is used, whereas they are between -0.45 to 0.45 m/s with the upstream model. The new scheme is less damping than the upstream scheme and this means that the reflection at the boundaries is much more pronounced. Prior to including the upper boundary condition presented earlier, the grid was staggered with the Arakawa C-grid. The staggered model gives a much smoother vertical wind field, Fig. 6b, and the maximum values become about the same as with the old upstream model. The upstream wave in the temperature field is about as evident as before, perhaps most distinct in isolines number five and eight, Fig. 6a. If the upper boundary condition is applied, the upstream disturbance is gone, Fig. 7a. The vertical wind velocity is somewhat smaller but the general features are the same, Fig. 7b. The extreme values in the temperature fields were about the same for all the simulations. In other words, similar results are obtained with the staggered model using the new advection scheme and the new upper boundary condition as with the old model. The advection process itself is, however, more accurately described.

4.5. *Results with Sea Breeze Simulations*

When the flow over bell-shaped terrain was studied the result with the new advection scheme was very similar to the

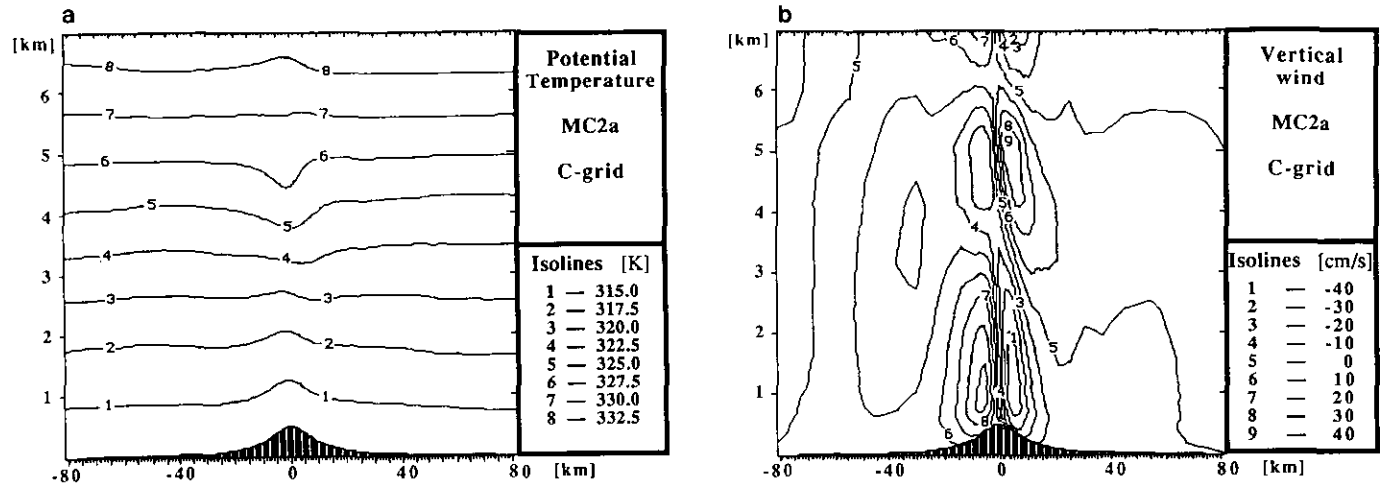

FIG. 6. (a) Same as Fig. 5a but with the C-grid. (b) Same as Fig. 5b but with the C-grid.

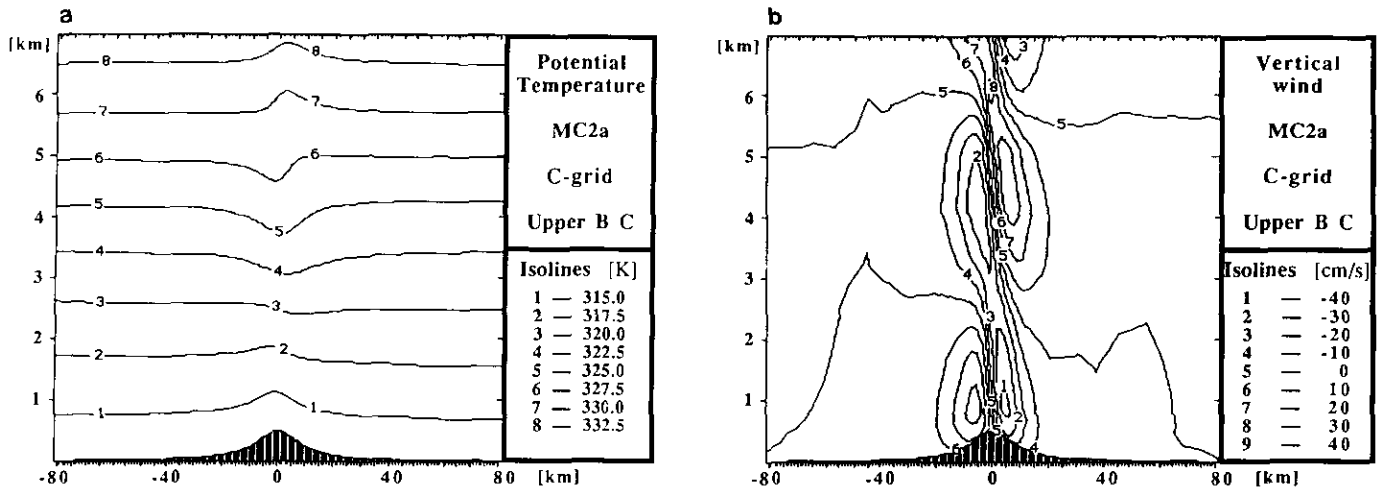

FIG. 7. (a) Same as Fig. 6a but with the upper boundary condition applied. (b) Same as Fig. 6b but with the upper boundary condition applied.

result with the old upstream scheme. That is also what can be expected, as advection is not the primary physical process in creating a vertical gravitational wave above the terrain. In this subsection a major difference between the schemes will be demonstrated. Just as in the flow over the bell-shaped terrain case the total model domain height was 7 km, but the simulated sea breeze circulation occurred below about 2.5 km which is why the figures only show that part of the fields. Both the $2\Delta x$ and $4\Delta x$ waves were filtered.

Reference [15] simulated idealized sea breeze systems with the MIUU model over islands of different sizes. When the scale of the land surface was relatively small, the two initial sea breeze systems, originating near the shores, merged into a quite a strong convergence zone over the island's center. When the scale was extended to about 100 km or more, that did not occur. Here we study the development of sea breeze over an island which has a width of 170 km. The grid distance is 10 km and the simulation is performed in two dimensions, corresponding to an infinitely long island in the north–south direction.

The 20 vertical levels are situated according to Eq. (27), with the lowest gridpoint above ground at 2 m. The initial lapse rate of potential temperature is 4 K/km. The geostrophic wind is set to zero, numerically 1 cm/s, corresponding to a calm free atmosphere. The surface roughness length z_0 is 5 cm over land and 0.2 mm over sea. The surface temperature is initially 288 K at all gridpoints, but after sunrise the temperature over the island is increased by H, which is defined as

$$H = 8 \sin(\pi/2\, t/6), \tag{55}$$

where t is the time in hours after sunrise. The heating has thus its maximum 6 h after sunrise. In the simulations sunrise is at 6 am and the maximum heating is at noon. The heating over land is then kept constant throughout the rest of the simulation until 4 pm.

In a sea breeze circulation system horizontal cross sections of one of the parameters, e.g., the vertical wind field or potential temperature field, are normally studied. Here we are more interested in the sea breeze front, and a good way to study that is to look at how the horizontal velocity at a fixed point changes with time. In Figs. 8 and 9 the horizontal wind speed at a point 30 km from the shore line is shown for simulation with the two advecion schemes. The new advection scheme, Fig. 8, gives a sharp maximum at about 1 pm of somewhat more than 5.5 m/s. The upstream scheme on the other hand, Fig. 9, gives a wind speed that is less than 5 m/s and, furthermore, the maximum is delayed about 1 h,

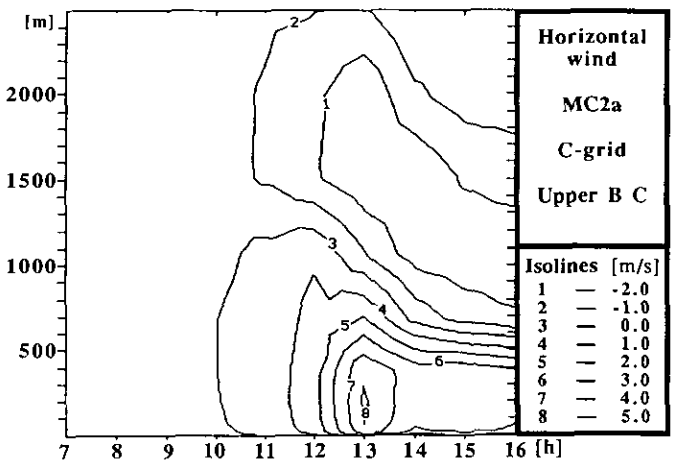

FIG. 8. The development of the horizontal wind component perpendicular to the shore line at a point 30 km inland from the shore line as simulated with the new advection scheme MC2a. The width of the island is 170 km. The initial lapse rate $d\Theta/dz$ is 4 K/km and the geostrophic wind speed is set to zero.

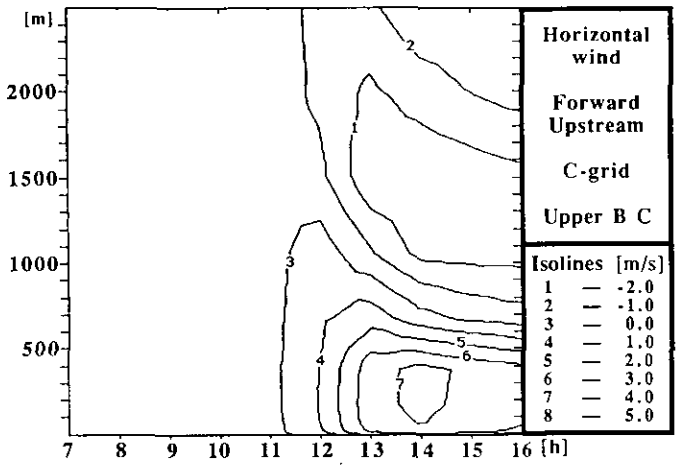

FIG. 9. Same as Fig. 8 but with the forward-upstream scheme.

compared to the new advection scheme. The maximum values of the wind component going in the other direction, from land towards the sea are about the same in both simulations, somewhat less than 2.5 m/s.

5. CONCLUSIONS

The advection scheme presented in this paper is shown to be superior to the upwind scheme when it comes to simple linear advection. It also gives a better solution in a non-linear case, the physically relatively simple model of the shock wave. When we look at the more complex case of a two-dimensional atmospheric model it is much harder to explicitly point out the improvements due to the higher order advection scheme, as there are so many other physical processes going on at the same time. The simulation of the sea breeze front has a lot in common with the shock wave. The front is much sharper and has a higher maximum value with the new scheme. The maximum is reached earlier in the simulation. In the flow over the bell-shaped terrain case the new advection scheme gives about the same solution as the upwind model does. Hopefully this new scheme represents the advection process better also in this more complex case. The advection process itself is physically less important here than in the sea breeze simulation. The major drawback of the new scheme is, of course, that it demands quite a bit more computer time, not due to the advection scheme itself, but because we have to incorporate more numerical filtering and a new upper boundary condition that allows vertically propagating gravity waves to pass through the upper boundary and not to reflect down into the model again. As this upper boundary condition uses fourier transforms it is even heavier in a fully three-dimensional atmospheric model. In three dimensions the model without a filter takes about the same time with the two different schemes, in fact a little less with the new scheme, as the new scheme is independent of the wind direction. If we are using the $2\Delta x$ filter it almost takes twice as much time with the new scheme and, if we are also using the $4\Delta x$ filter, the time spent in the program is about three times as much as with the original forward-upstream scheme. Still, if we want to have a numerical model for the atmosphere it is very important to have an advection scheme as accurate as possible, especially if we want to be able to model dispersion processes along with the ordinary physics of the atmosphere.

One reason for the combination of a telescopic grid transformation and the damping forward-upstream scheme in the old model was to keep the influence from disturbances at the boundaries as small as possible while maintaining reasonable accuracy in the central domain of the model located over the area of main interest. The flow over the bell-shaped terrain case shows that in a theoretical study with relatively smooth terrain the result from the old model is as accurate as the new model when it comes to the dynamics. In some applications a combination of the two different advection schemes may be advantageous, with the old scheme for the dynamics and the new scheme for parameters where advection is one of the most important physical mechanisms. A combination with different advection schemes in the different directions is also a possible course of action. If the meso-γ-scale model is nested within a larger scale model it is important to ensure that all relevant information from the larger model, which is implemented at the boundaries of the meso-γ-scale model, will affect the whole domain of the inner model.

ACKNOWLEDGMENTS

The author is very grateful to Professor Per Lötstedt at the Department of Scientific Computing, Uppsala University for fruitful discussions and advice. Thanks also to my other supervisors, Professor Ulf Högström and Dr. Leif Enger and all other colleagues at the Department of Meteorology, especially Drs. Anders Andrén, Michael Tjernström, Xiaohua Yang, and Ms. Gunilla Svensson. Last but not least, my sincere thanks and love to my family.

REFERENCES

1. R. B. Rood, *Rev. Geophys.* **25**, 71 (1987).
2. D. P. Chock, *Atmos. Environ. A* **25**, 853 (1991).
3. A. J. Gadd, *Q. J. R. Meteorol. Soc.* **104**, 583 (1978).
4. A. J. Gadd, *Q. J. R. Meteorol. Soc.* **106**, 215 (1980).
5. K. M. Carpenter, *Q. J. R. Meteorol. Soc.* **107**, 468 (1981).
6. W. G. Collins, *Q. J. R. Meteorol. Soc.* **109**, 255 (1983).
7. R. W. MacCormack, in *Proceedings, Second International Conference on Numerical Methods in Fluid Dynamics*, Lecture Notes in Physics, Vol. 8 (Springer-Verlag, New York, 1971).
8. H. T. Mengelkamp, *Boundary Layer Meteorol.* **57**, 323 (1991).

9. H. Kapitza and D. P. Eppel, *Beitr. Phys. Atmosp.* **65**, 23 (1992).
10. A. Grammeltvedt, *Mon. Weather Rev.* **97**, 384 (1969).
11. G. A. Sod, *J. Comput. Phys.* **27**, 1 (1978).
12. C. K. Forester, *J. Comput. Phys.* **23**, 1 (1977).
13. M. Tjernström, L. Enger, and A. Andrén, *J. Theor. Appl. Mech.* **7**, 167 (1988).
14. A. Andrén, *J. Appl. Meteorol.* **29**, 224 (1990).
15. X. Yang, *Boundary Layer Meteorol.* **54**, 183 (1991).
16. X. Yang, *Boundary Layer Meteorol.*, submitted.
17. L. Enger, D. Koracin, and X. Yang, *Boundary Layer Meteorol.*, submitted.
18. F. Mesinger and A. Arakawa, WMO/ICSU Joint Organizing Committee, GARP Publ. Ser. 17, (GARP, Geneva, 1976).
19. J. B. Klemp and D. R. Durran, *Mon. Weather Rev.* **111**, 430 (1983).
20. A. Eliassen and E. Palm, *Geophys. Publ.* **27**, 1 (1960).
21. P. Queney, *Bull. Am. Meteorol. Soc.* **29**, 16 (1948).